Electric-Double-Layer Oriented Field-Screening Effect on High-Resolution Electromechanical Imaging in Conductive Solutions

Yan Ye (叶艳),[1] Anyang Cui (崔安阳),[1] Liangqing Zhu (朱亮清),[1] Zhigao Hu (胡志高),[1,2,3,*] Kai Jiang (姜凯),[1] Liyan Shang (商丽燕),[1] Yawei Li (李亚巍),[1] Guisheng Xu (许桂生),[4] and Junhao Chu (褚君浩)[1,3]

[1] *Technical Center for Multifunctional Magneto-Optical Spectroscopy (Shanghai), Department of Electronic Engineering, East China Normal University, Shanghai 200241, China*

[2] *Collaborative Innovation Center of Extreme Optics, Shanxi University, Taiyuan, Shanxi 030006, China*

[3] *Shanghai Institute of Intelligent Electronics & Systems, Fudan University, Shanghai 200433, China*

[4] *Key Laboratory of Transparent Opto-Functional Advanced Inorganic Materials, Shanghai Institute of Ceramics, Chinese Academy of Sciences, Shanghai 201899, People's Republic of China*

(Received 24 April 2019; revised manuscript received 13 August 2019; published 4 September 2019)

Complex electrical behavior, including the field-screening distribution and possible electrochemical effects, makes electromechanical imaging by piezoresponse force microscopy in conductive liquids a critical challenging issue in studying the functionalities and performance of piezoelectric materials. Here, we propose a theoretical model to directly quantify the electric-field-screening effect inside the tip-sample junction in a variety of electrolytes of varying ionic strength. The field-screening effect resulting from an electric double layer in the tip-surface system offers the benefit of better understanding of the central physical mechanism in electrical probing by scanning probe microscopy (SPM) in a polar liquid medium. Experimentally, an intrinsic piezoresponse in ferroelectric antiparallel-polarization regions is observed in electrolytes with various assemblies of valences and with various molarities through updating the design of a nanoelectrode probe. Accompanied by the unveiling of the underlying physical mechanism, these experimental results pave the way to the broad application of *in vivo* or *in operando* electrical analysis on the nanoscale by the SPM technique in conductive-liquid environments.

DOI: 10.1103/PhysRevApplied.12.034006

I. INTRODUCTION

Electrical characterization in liquid environments is of great importance to revealing the fundamental mechanisms in and the performance of functional materials [1–3] and energy nanodevices [4], and is also of great importance in biological research [5]. The need for further understanding of material properties and of mechanisms in systems on the nanoscale is driving us to apply scanning probe microscopy (SPM) in liquid environments. Domanski *et al.* applied Kelvin-probe force microscopy in a liquid to investigate the work function of a gold interface upon chemisorption of hexadecanethiol [6]. Boettcher *et al.* reported that the surface electrochemical potential of electrocatalysts *in operando* could be sensed by electrochemical atomic force microscopy in an aqueous $Co(NO_3)_2$ solution [7]. Therefore, researchers are expecting to utilize advanced techniques for *in operando* analysis of electronic and electrochemical materials and devices to uncover real-time performance and to further understand fundamental mechanisms.

As a state-of-the-art technique, piezoresponse force microscopy (PFM) is a contact voltage-modulated SPM mode and is becoming a versatile tool to characterize electromechanical phenomena on the nanoscale [8]. Electromechanical coupling, which is one representative electrical property, is ubiquitous in a wide range of materials and systems, such as ferroelectrics [9], solar cells [10], ion batteries [11,12], bioelectronics [13,14], and biopiezoelectric systems [5]. Hence, PFM is applicable not only to investigating the nondestructive visualization and control of ferroelectric nanodomains [15–18], but also to measuring the piezoresponse of biological cells and tissues [19–21] in ambient environments. Moreover, several attempts have been made to apply the PFM technique in liquid environments to probe ferroelectric domains [22–26] and to characterize biological piezoresponses [27–29]. It is common knowledge that working in an aqueous medium can reduce the long-range electrostatic contributions to the signals detected. PFM in a liquid environment allows one to have precise control of the

*zghu@ee.ecnu.edu.cn

tip-surface interaction by eliminating the capillary forces caused by humidity of the air and by reducing van der Waals forces, so that it can improve the imaging resolution and sensitivity [22,23]. PFM in a liquid could also localize the ac and dc fields, which is critical to other operations in techniques used with liquids [30]. In consequence, there is extensive interest in applying the PFM technique in aqueous environments to visualize surface polarization with high resolution, measure underwater electrical devices in natural environments, and sense *in vivo* electroactivity in biological systems.

Unfortunately, it is extremely challenging to apply electrical SPM characterization in a conductive liquid environment, due to the complicated electric-field distribution and possible electrochemical reactions. Even if the latter electrochemical reactions are avoided by controlling the testing bias, voltage-induced ionic electromigration in electrolytes leads inevitably to the formation of electric double layers (EDLs) near the charged surfaces of the tip and sample [31]. The electric-potential drop across the EDL structure screens efficient interactions of the electric field between the tip and sample [22,23,32]. This phenomenon at the tip-surface junction in liquids, also called the field-screening effect or Debye-screening effect, still restricts the application of high-resolution electrical probing of functional materials and electrical devices in highly conductive liquids. Notably, the field-screening effect results in poor performance of electromechanical imaging by PFM in conductive solutions. Balke *et al.* performed pioneering research in which they discussed electromechanical visualization in liquids by the use of an equivalent-circuit method [25]. Therefore, the structure of the EDLs in the tip-sample system and the corresponding electrical behavior are still regarded as one of the key aspects that control the capability of electrical probing in conductive environments. It is necessary to explicitly investigate further the physical nature of the EDL oriented field-screening effect on PFM visualization in electrolytes.

Here, we employ the finite element method to systematically simulate the potential distribution between a biased tip and a charged sample surface, as well as illustrate the field-screening effect resulting from ionic electromigration in conductive solutions. For comparison with the theoretical analysis, a series of PFM images on the nanoscale shows high-resolution ferroelectric nanodomains in electrolytes of molarity less than 100 mM. A strong field-screening effect leads to poor imaging in solutions of higher ionic strength. The numerical models and experimental visualization focus mainly on deionized H_2O, glucose solution, and electrolytes with various valences and concentrations of anions and cations involving Na^+, K^+, Cu^{2+}, Mg^{2+}, Cl^-, SO_4^{2-}, and PO_4^{3-}. This work is expected to promote the development of electrical characterization by SPM in highly conductive environments, and could motivate researchers to use advanced SPM electrical techniques for *in vivo* or *in operando* analysis in the areas of functional materials, underwater electrical devices, electrochemical systems, and bioelectronics.

II. SIMULATIONS OF FIELD-SCREENING EFFECT

In terms of electromechanical probing, a PFM mode is developed to detect picometer-scale piezoelectric deformation on the sample surface, based on the converse piezoelectric effect. When the conductive tip is brought into contact with the sample surface, an ac voltage $V_{ac} = V_{dc} + V_0 \cos(\omega t)$ is applied to the tip using a functional generator [8,33]. A schematic of the PFM setup in a liquid environment is shown in Fig. 1. Actuated by the ac electric field, a shift of the positive and negative charge centers in a ferroelectric or piezoelectric material takes place, resulting in picoscale deformation on the surface [34]. Then, a force on the tip induced by the deformation is read out as a displacement of the cantilever with the use of a lock-in amplifier. At the same time, the inherent spontaneous-polarization property of a ferroelectric material is expected to contribute to the bound charge accumulated at the (001) crystal surface [35]. In this case, once the surface of the tip or sample is exposed to a liquid, it is charged through the ionization of surface groups or by the adsorption of ions from the solution. Some ions in the liquid are bound to the surface, and some are in rapid thermal motion, forming an ionic cloud near to the surface [36,37]. The EDL structure consists of a compact Stern layer and a diffuse layer, where the Stern layer is regarded as one capacitance of a parallel-plate capacitor. The Gouy-Chapman-Stern model of the EDL has been widely acknowledged as explaining the dynamics of the electrode-electrolyte interface [30,38]. As shown in Fig. 2(a), hydrated counterions are absorbed on the tip and the sample surface, constituting the inner Helmholtz plane (IHP) and outer Helmholtz plane (OHP). Note that a linear drop in electric potential occurs across the Stern or Helmholtz layer, whose thickness is only of the order of a few angstroms. The potential distribution [$\psi(x)$] in the diffuse layer complies with the Poisson-Boltzmann

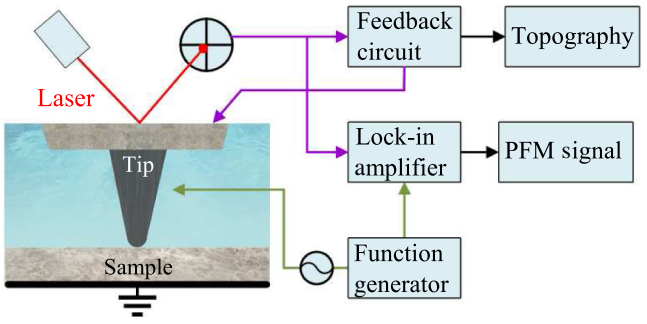

FIG. 1. Schematic of the setup for piezoresponse force microscopy in a liquid environment.

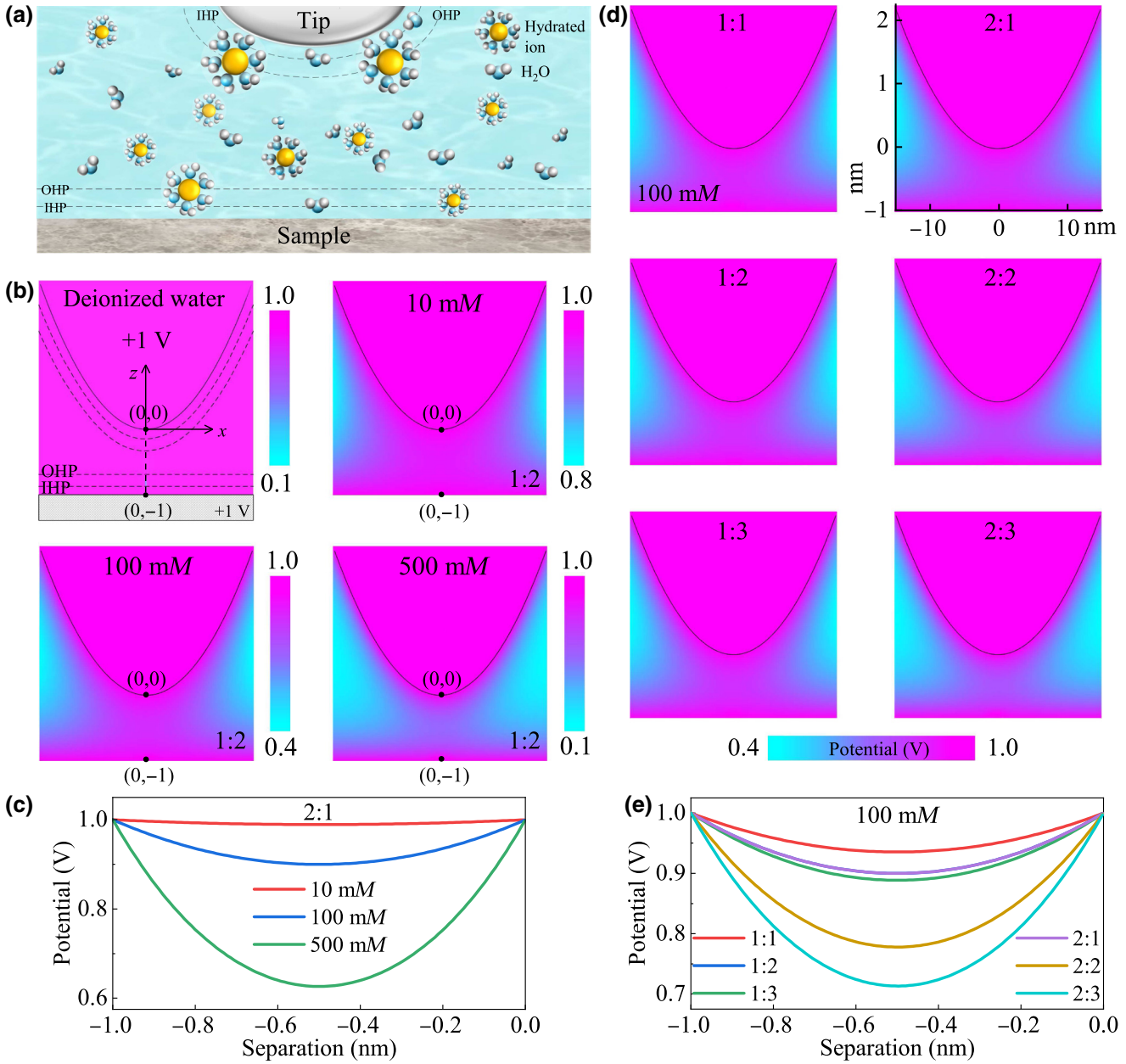

FIG. 2. Numerical simulation of electric-potential distribution in the tip-surface junction. (a) Idealized schematic of EDL structure, including the IHP and OHP formed on the tip and the sample surface. (b) Electric-potential distribution between the tip and the sample surface in deionized water and in 10, 100, and 500 mM solutions for valences 1:2. We define coordinates (x,z), where the tip vertex is regarded as the origin $(x=0,z=0)$. The x axis is the coordinate parallel to the sample surface. The z axis is perpendicular to the sample surface. The color threshold of the potential mapping in the color bars is adjusted from 0.8 V (10 mM) to 0.1 V (500 mM) in order to adapt to the increasing screening effect while providing a clear view. (c) Drop of electric potential between tip and sample with distance z in solutions of different molarity for given valences 1:2. By means of theoretical simulation, the potential distributions are also modeled (d) for 100 mM with a variety of valences. (e) Lines showing the behavior of the potential distribution between the tip and sample in 100 mM solutions with different valences.

equation,

$$\nabla^2\psi(x) = \sum_{i=1} -\frac{z_i e c_i}{\varepsilon_0\varepsilon_r}\exp\left(\frac{-z_i e\psi(x)}{k_B T}\right), \qquad (1)$$

where k_B is the Boltzmann constant, ε_0 and ε_r are the dielectric constants, c_i is the bulk molar concentration far away from the surface, z_i is the valence, T is the absolute temperature, and e is the elementary charge. The potential decreases exponentially on crossing the diffuse layer,

whose characteristic length or "thickness" is quantified by the Debye length (λ_D). The value of λ_D decreases according to the equation

$$\lambda_D = \sqrt{\sum_{i=1} \frac{\varepsilon_0 \varepsilon_r k_B T}{c_i z_i^2 e^2}} \tag{2}$$

as the valence and molarity of the electrolyte increase. Obviously, it depends only on the properties of the liquid, and not on the surface properties of the sample such as charges and potentials at certain temperatures. Moreover, the valence and concentration of ions in solutions together define the ionic strength $I = \frac{1}{2}\sum_{i=1} c_i z_i^2$. The Poisson-Boltzmann equation is accordingly simplified by the approximation $-z_i e\psi(x)/k_B T \ll 1$ of the Debye-Hückel theory to $\nabla^2\psi(x) = \lambda_D^{-2}\psi(x)$, which is available for arbitrary electrolytes [38].

As the two EDLs at the tip and the sample surface overlap with each other, the EDL interaction force has to be considered. The tip-surface system can be treated as a sphere of radius R near a flat surface (of unit length). Invoking the Derjaguin approximation [36], the EDL force in the sphere-flat model is

$$F_{\mathrm{EDL}} = \kappa R Z e^{-\kappa h}, \tag{3}$$

where κ is the inverse Debye length, h is the separation of the tip and surface, and Z is the interaction constant, defined as $Z = 64\pi\varepsilon_0\varepsilon(kT/e)^2\tanh^2(ze\psi_0/4kT)$. The EDL interaction force has been reported by Ferris *et al.*, who made great progress in studying the EDL force as a function of separation distance by using colloidal-probe force microscopy [39]. Additional studies have introduced quantitative measurements of charge density on biological molecules through using EDL force measurements [40–42]. The EDL interaction force, considered as an electrostatic coupling, participates in a portion of the electrical and mechanical interactions in PFM imaging considered in the experimental section (Sec. III).

Also, during SPM measurements in liquids, a dead layer is generally considered to exist and to separate the tip and the sample surface; it arises mainly from a low-polarizability layer of surface adsorbates or from interaction between hydrophobic and hydrophilic surfaces [22,23,25,32]. Previous investigations have studied the thickness of the dead layer as a function of voltage and found that a thickness of around 2.7 nm with a low dielectric constant matched the imaging quality of PFM visualization [25]. In addition, anions or cations in polar solutions usually bind 4–6 water molecules to form hydrated ions, whose radii are less than 0.5 nm [36,43]. Therefore, we take the dead layer into consideration in the following simulation and demonstrate the presence of a separated layer in the theoretical and experimental results. In the present simulation, we reasonably hypothesize that the thickness of the dead layer (h) is either 1 or 3 nm between the tip apex and the sample surface.

Additionally, it is necessary to have a clear description of the dynamics of mobile ions, as the application of PFM is based on frequency-dependent modulation. Once a voltage is applied to the tip-surface junction, mobile ions undergo electromigration in response to the applied electric field. In fact, when the molarity of the electrolyte is over 1 mM, the drive voltage $V_{\mathrm{ac}}(\omega)$ would require a frequency range higher than 10^7 Hz to cause the ions to be in quasistatic equilibrium [44]. This range has almost not been reached, and is beyond the limitations of the frequency range in available commercial SPM systems. Otherwise, there is a rich landscape for mobile ions under the $V_{\mathrm{ac}}(\omega)$ bias to periodically form an EDL structure and screen the effective electromechanical interactions within the drive-frequency space (10^3–10^5 Hz) in the overwhelming majority of PFM applications.

We put forward a numerical model to simulate the field-screening effect by the finite element method. The model is based on Eq. (1), simplified by the Debye-Hückel equation $\nabla^2\psi(x) = \lambda_D^{-2}\psi(x)$, where, consequently, the model is presented based on cylindrical coordinates (r, z)) as $\partial^2\psi/\partial r^2 + (1/r)(\partial\psi/\partial r) + \partial^2\psi/\partial z^2 = \lambda_D^{-2}\psi(x)$. The boundary conditions are based on Neumann and Dirichlet boundary types. In the model, the tip apex is regarded as a constant momentary potential of +1 V, and the tip radius is 25 nm. Considering bound charges on the surface arising from spontaneous polarization, we also set the sample surface to be at +1 V in the simulation. The potential distribution in the three-dimensional structure of the tip-liquid-surface system [Fig. 2(a)] is shown in a cross section of the tip-sample junction. The thickness of the dead layer between the tip and the sample surface is first hypothesized as 1 nm. In deionized water, as shown in Fig. 2(b), the electric potential is distributed uniformly in the tip-surface junction. The electric field, with no potential reduction, cannot be screened by the EDLs and is global within the tip-surface junction; the Debye length in deionized water is about 960 nm at 25 °C. Hence, it is feasible to probe electromechanical interactions in deionized water.

In parallel, simulations are performed for various assemblies of valences (1:1, 1:2, 1:3, 2:1, 2:2, and 2:3) in 10, 100, and 500 mM solutions to evaluate the spatial variation of the potential. Owing to the formation of an EDL, the potential decreases exponentially on the scale of the Debye length in these ionic solutions. The liquid around the tip and the sample is at a lower potential than the tip and the sample themselves. When the molarity is increased from 10 to 500 mM for 1:2 electrolytes [Fig. 2(b)], the behavior of the potential in the tip-surface junction shows an increasing reduction, corresponding to the stronger screening effect in solutions of higher concentration. To clearly illustrate the spatial variation of the behavior of the electric potential in the space ($h = 1$ nm) between the tip and

surface, the potential profiles as a function of distance are highlighted below the tip apex. We define coordinates (x, z) with the z axis perpendicular to the sample surface and the x axis parallel to the sample surface. The tip vertex is taken as the origin (0, 0) of the coordinates, and the spot on the sample surface below the tip is taken as (0, −1) in Fig. 2(b). As displayed in Fig. 2(c), a higher ionic concentration of the electrolyte leads to a steeper decay in potential for the given valences 1:2, where the potential decreases by about 38% at the middle of the tip-surface separation in a 500 mM electrolyte, and by about 10% in a 100 mM one. Comparing the spatial variation of the potential in high-molarity and low-molarity electrolytes, we see that the reduction in the potential enables the delivery of the electric field to be interrupted severely between the tip and the sample surface. This can be ascribed to the fact that a higher concentration corresponds to a thinner thickness of the EDL structure and a stronger ionic strength.

Another parameter of the ionic strength that is important in determining the thickness of the EDL structure is the valence, according to Eq. (2). The potential distribution in electrolytes with different assemblies of valences is modeled and is shown for molarities of the electrolyte of 100 mM in Figs. 2(d) and 2(e), and for 10 and 500 mM in Fig. 6 (see Appendix A). A larger sum of valences of the anions and cations is associated with more reduction in the potential distribution. The situations of 1:2 and 2:1 assemblies correspond to almost the same profile of potential. The progressive decay is severer for the 2:3 type of electrolyte than for electrolytes of low-valence type, even though the molarities of all electrolytes are controlled at 100 mM in Fig. 2(f). The Debye length is also smaller for 2:3 electrolytes. In other words, electrolytes with a high ionic strength alter the potential in the local distribution in the tip-surface junction and bring about some difficulties in the electromechanical interactions. The electromechanical response (P_{em}) obtained during a PFM experiment in an ambient or liquid environment can be depicted as $P_{\mathrm{em}} = \alpha_a(h)\widetilde{d}_{33}(k_1)/(k + k_1)$, where $\widetilde{d}_{33}$ is the intrinsic electromechanical response of the sample, $\alpha_a(h)$ is the ac-potential ratio of the tip to the sample surface, h is the separation of the tip and sample, and k_1 and k are the spring constants of the tip-surface junction and the cantilever, respectively [23,32]. In a liquid environment, the consideration of the tip-surface junction should take the effect of the liquid layer and the gap between the tip and sample into consideration. The screening coefficient is $\alpha_a(h) = 1$ for $h \ll \lambda_D$ when the tip is in contact with the sample in liquid, and $h \leq 0$ in air. However, if the EDLs around the tip and surface do not overlap, the value of $\alpha_a(h)$ is 0. The reduction in the value of the $\alpha_a(h)$ ratio is attributed to an electric-double-layer oriented field-screening effect in electrolytes. Therefore, the electromechanical interaction in the tip-sample junction shows a gradual decrease in solutions at distances on the scale of λ_D for the solution, according to the simulation results.

The simulation results prove that the field-screening effect becomes stronger with increasing ionic strength ($I = \frac{1}{2}\sum_{i=1} c_i z_i^2$). Since the thickness of the gap between the tip and the sample surface is enough to contain the entire EDL structure ($\delta > 2\lambda_D$), the electrical interaction has to be blocked due to the strong field-screening effect. Therefore, the inverse piezoelectric interaction cannot work properly in highly conductive liquids. In this case, PFM is incapable of detecting piezoresponse signals. In short, the models given indicate that the electromechanical interactions are reduced on a scale of the magnitude of the Debye length in solutions as the ionic strength is increased. We cannot be sure that the dead layer has a fixed size in reality, although its thickness is generally considered to be from a few angstroms to several nanometers [22,23,25,32]. Thus, the numerical simulations also consider the modeled behavior of the potential when the thickness of the dead layer is set as 3 nm. As shown in Fig. 7 (see Appendix A), the field distribution in a 3-nm separation between the tip and the sample surface exhibits a screening effect similar to that in the 1-nm gap addressed above. A higher valence and concentration would create a stronger field-screening effect, associated with increased difficulty in PFM mapping in highly conductive liquid environments. But, as the thickness of the dead layer increases, the threshold of the ionic strength of the imaging solution is limited. In some special cases, the observed sample surface may be treated as being at 0 V without a surface charge. Figure 8 in Appendix A also presents theoretical results for the field-screening effect where the voltage (+1 V) is applied only to the tip and the sample surface potential is set as 0 V for electrolytes of different concentrations and with different assemblies of valences. The trend in the potential attenuation is also similar to the results in Figs. 2, 6, and 7 (see Appendix A), which illustrates that the field-screening effect is a key factor for PFM in liquids.

III. ELECTROMECHANICAL IMAGING IN ELECTROLYTES

An electric-field-screening effect in the tip-surface junction could exist extensively for the different electrical probing modes of SPM. Owing to the weak piezoresponse at the picometer scale in most materials, the PFM method uses a lock-in amplifier to enlarge the intrinsic piezoresponse. Thus, probing the piezoresponse in aqueous conductive media is generally considered an enormous challenge. A type of nanoelectrode probe with an insulated cantilever is applied to perform piezoelectric measurements in conductive liquid environments. A scanning electron microscopy (SEM) image [Fig. 3(a)] shows an enlargement of the geometry of the nanoelectrode tip, where the Pt-coated tip apex is conductive and the

remaining part is fully isolated by dielectric materials. The diameter of the tip apex is about 43.4 nm, and a three-dimensional schematic of the tip in a liquid is also shown in Fig. 3(b). Compared with a traditional metal-coated probe, the unique structure of this nanoelectrode probe is beneficial for imaging more precisely and reducing the stray current in liquids [45]. The nanoelectrode probe has been applied to investigate electrical properties in polar liquids, showing outstanding behavior [46,47]. To validate the field-screening effect during PFM imaging in liquids, antiparallel polarizations of a ferroelectric $Pb(In_{1/2}Nb_{1/2})O_3$-$Pb(Mg_{1/3}Nb_{2/3})O_3$-$PbTiO_3$ (PIMNT) single crystal are imaged in air, deionized water, and K_2SO_4, Na_3PO_4, $CuCl_2$, $MgCl_2$, $MgSO_4$, and glucose solutions with concentrations of 1, 10, and 100 mM, as shown in Fig. 3. A fingerprintlike domain pattern, self-assembled by polar nanoregions (PNRs), can be seen in Fig. 3(c); a PNR structure in the PIMNT lattice has been reported many times [48–50]. The lattice structure of PIMNT is demonstrated by Raman spectroscopy and x-ray diffraction, as reported in Appendix B. The slight differences in the ferroelectric domain patterns in PIMNT single crystals can be attributed to stress accommodation and random fields, which are sensitive to the PT compositions.

Figures 3(d) and 3(f) show amplitude images of the piezoresponse in ambient and aqueous environments, respectively. The cross talk in the PFM signal in air is partially affected by the long-range electrostatic force due to capacitance, because of the sample topography [29]. The amplitude in air [Fig. 3(d)] is slightly superimposed by topographic cross talk, which cannot be found in the amplitude image in DI water [Fig. 3(f)]. In the ambient environment, both the long-range electrostatic interactions and the electromechanical interactions participate in electromechanical visualization by PFM. In contrast, the mobile ions and solvent molecules in solutions are beneficial for screening the long-range electrostatic interactions between the tip and surface. It can easily be understood that the electrostatic interactions decay exponentially across the EDL structure at a solid-liquid interface when the minimized separation h is greater than the Debye length, i.e., $h > \lambda_D$, unlike the case in air [23,29]. Furthermore, capillary interaction in the tip-surface junction severely limits the resolution of PFM probing in air as well, and decreases the observed width of domain walls. In an aqueous environment, the lack of capillary interaction can improve the lateral resolution of ferroelectric domains.

Out-of-plane PFM phase images involving antiparallel domains are recorded in various solutions with valence assemblies of 1:2, 1:3, 2:1, and 2:2 and with molarities from 1 to 100 mM at one nonresonant frequency. For a single-frequency PFM mode, a drive frequency near the contact resonance may lead to cross talk, with surface morphology superimposed on the enhanced piezoresponse signals. On the other hand, a high ac voltage may induce electrochemical interactions such as the formation of bubbles (water splitting), which have negative effects on the electromechanical interaction. A controlled drive amplitude of less than 5.5 V is applied in our experiments, because it has been proved that a modulation amplitude of less than 5.5 V can effectively avoid water splitting [26]. Figure 3(g) enlarges the phase images observed in varied kinds of electrolyte. The phase response is used to yield binary information (−90° to +90°) about the surface-polarization

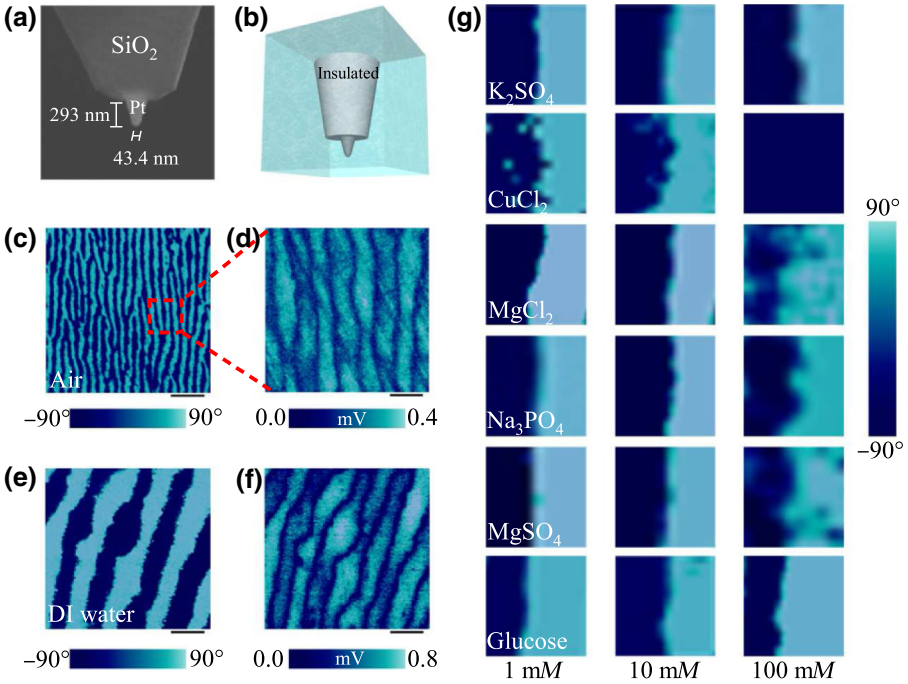

FIG. 3. Electromechanical imaging in different electrolytes. (a) SEM image of the nanoelectrode tip. The diameter of the tip apex is about 43.4 nm. (b) Three-dimensional schematic of the tip-apex structure in the solution. (c) Fingerprintlike domain pattern in PIMNT observed in ambient environment. The scale bar is 2 μm. (d) Amplitude image (1 μm^2) of PIMNT enlarged from (c). (e) Phase and (f) amplitude images obtained in deionized (DI) water. The scale bar is 200 nm. (g) Phase images involving antiparallel domains measured in various kinds of solution. The image size is 200 nm.

status, and determines the position of domain walls. Obvious phase contrasts of about 180° and sharp edges are achieved in 1 and 10 mM solutions. However, the edges of domains are blurred and the signal-to-noise ratio decreases in 100 mM electrolytes due to the electromechanical interaction being blocked by the stronger field-screening effect, just as the theoretical prediction suggests. Owing to the phase-optimization mechanism of the PFM based on digital lock-ins of the controller, the phase contrast is not lost much in solutions with high molarity. The phase-optimization mechanism in the PFM system allows for and corrects the oscillation of the observed phase signal and slight noise interference by examining the difference in the signal vectors between the input phase signal of the modulation and the surface deformation.

Although the electric-potential drop is different for different valences, the phase images do not show much diversity with changing valence. Therefore, this result of robust phase contrast confirms that the PFM system is suitable for electromechanical imaging in electrolytes of molarity up to 100 mM, which can be attributed to the narrow "channel" in the tip-sample junction formed by the overlapping EDLs, as shown in Figs. 2(b) and 2(d), and in Figs. 6(a), and 7(a) in Appendix A. This "channel" implements the interaction, including the effective electromechanical interaction and the EDL interaction. Without the overlap of EDLs in high-molarity electrolytes [see the simulation results for 500 mM solutions in Figs. 6(b) and 7(c)], the effective electromechanical interaction, EDL interaction, and even electrostatic interaction would be blocked between the tip and the surface. Then, the phase-optimization mechanism would have no signal to collect and optimize, due to the lack of interactions. Hence, it seems to be difficult to probe electromechanical coupling in solutions of over 500 mM owing to the serious field-screening effect. For comparison with a liquid environment without mobile ions, electromechanical visualization produces high-resolution phase images of about 180° contrast in glucose solutions, despite the concentration being increased to 100 mM. Nevertheless, it can be noted that failure of electromechanical detection in $CuCl_2$ solutions of molarity over 10 mM is ascribed to electrochemical reactions, which drive metallic Cu to precipitate out due to the oxidizability of Cu^{2+}. Thus, if water splitting is eliminated in the electrolyte, electrochemical reactions can still be extremely sensitive to the ion species in the electrolyte.

Then, we highlight the ability of electromechanical mapping with high spatial resolution on the molecular or cellular scale by collecting together the values of the lateral resolution of the observed domain-wall width. In reality, the measured width of a domain wall could be decided mostly by the tip radius; in the present work, this is about 22 nm, obtained from the SEM image shown in Fig. 3(a). In order to quantify the domain-wall width from the experimental data, the PFM signals are fitted with a modified function according to a widely applicable micromagnetic theory [51], $A(x) = A_l + (A_l - A_r)\tanh[(x - x_0)/(w/2)]$, where A_l and A_r are the responses on the two sides of the domain wall at x_0 [23,52]. Here, the PFM signal is a product of amplitude with phase, following the equation PFM signal = amplitude × sgn(phase) [53], where sgn is the sign function, used to determine the sign of the phase. We also normalize the PFM signals to an amplitude of 1. Figures 4(a)–4(e) show the fitted lines of the domain-wall

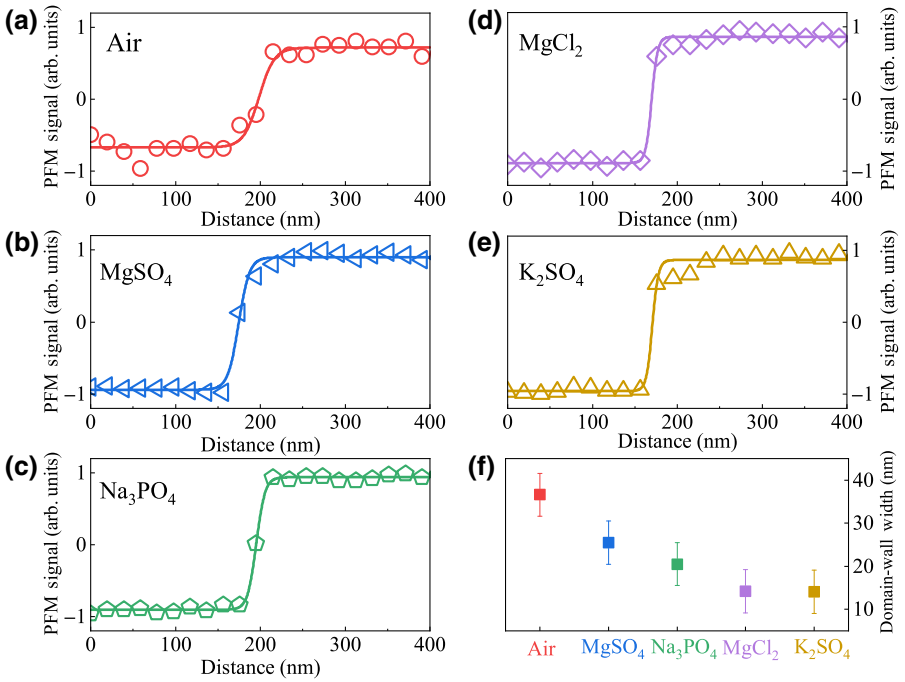

FIG. 4. Fitted domain-wall width observed in different conditions. (a)–(e) PFM signal profiles across a domain wall with fits (solid lines) in air, and in 1 mM K_2SO_4, Na_3PO_4, $MgCl_2$, and $MgSO_4$ solutions, respectively. (f) The value of every fitted domain-wall width with different electrolytes of molarity 1 mM.

profiles in air and in K_2SO_4, Na_3PO_4, $MgCl_2$, and $MgSO_4$ solutions of molarity 1 mM, for which the corresponding widths are about 36.4, 14.1, 20.5, 14.2, and 25.5 nm, respectively. Apparently, the domain-wall width measured in solutions with low molarity is less than that in air, from Fig. 4(f). When the ionic strength decreases, the domain wall becomes thinner. This can be explained by two effects: (i) the effective field-screening effect in electrolytes could cause the electric field to be concentrated in a smaller area below the tip apex than the actual tip radius; and (ii), as addressed above, the reduction of the electrostatic force and the elimination of capillary interaction in liquids further enhance the lateral resolution of the PFM amplitude. Hence, with higher ionic strength, the electric field, mostly screened by the EDL, fails to create an effective electromechanical interaction between the tip and the sample surface and is not enough to stimulate the piezoresponse of the material. Consequently, this brings about a difficulty in collecting the picometer-scale signal, which results in a loss of resolution in the PFM images.

Moreover, unexpected situations such as sample damage or tip wear could lead to poor performance of experiments when a large contact force is applied in PFM imaging. Thus, it is of great importance in applied high-resolution imaging to use minimal imaging force. Simultaneously, we doubt that the overlapping EDL structure would participate in the electrical or mechanical interaction between the tip and the sample surface in PFM detection, according to Eq. (3). As shown in Figs. 5(a) and 5(b), electromechanical probing is carried out with different contact forces in deionized water. The phase contrast and amplitude strength continue to show the ideal performance with a decrease in the force from 71 to −5 nN. Both signals reduce dramatically at −13 nN and eventually disappear at −22 nN. In the case of a positive force corresponding to a repulsive one, it can be understood why we obtain a perfect signal of the piezoresponse. What is noteworthy is that a robust piezoresponse is imaged with a negative (quasiattractive) force of −5 nN using a cantilever with a spring constant of 1.5 N/m and a calibrated deflection setpoint of −0.03 V. To show the spatial resolution in detail, Figs. 5(c) and 5(d) show enlarged images of the phase contrast, changing by 180°, obtained at 0 and −5 nN, respectively. In air, then use of an attractive (negative) force in PFM imaging is almost impossible to realize in contact mode. However, in a liquid environment, particularly one with mobile ions, the nonlocalized field contribution and EDL interaction may contribute to the characterization at 0 nN or a small negative force in deionized water. The EDL force is extremely difficult to quantify in PFM detection, but can be controlled by adjusting the ionic strength, pH, and temperature [54]. Therefore, it is possible to perform electromechanical testing at an interaction force of −5 nN with a contribution from the EDL interaction. While the increased negative force is much larger than the scale of the EDL force

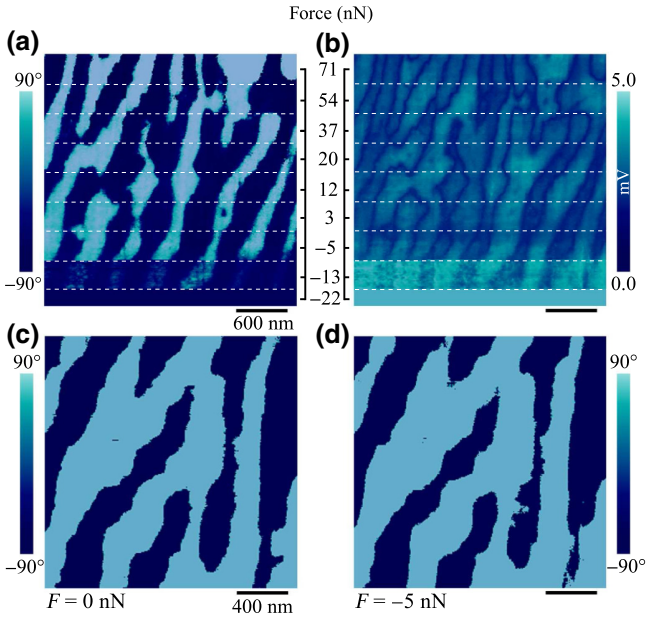

FIG. 5. (a) Phase and (b) amplitude images in DI water with various contact forces. Phase images achieved at contact forces of (c) 0 nN and (d) −5 nN.

[see as Eq. (2)], the tip will escape from the surface and have no interaction with the sample. We expect in the future to investigate the details of the overlapping fields and EDL interactions in SPM electrical characterization in conductive liquid environments.

IV. CONCLUSION

In summary, this work systematically reveals the field-screening effect in electromechanical probing by SPM in a series of liquid media, theoretically and experimentally. The numerical modeling explicitly describes the physical mechanism of the field-screening effect in conductive liquids. Moreover, the results of electromechanical imaging in numerous environments with assemblies of various valences and various molarities are consistent with the theoretical analyses. High-resolution images of ferroelectric domains are achieved in low-molarity solutions. However, a loss of resolution in electrolytes of molarity over 100 mM results from an enhanced field-screening effect. It is essential to characterize electromechanical coupling in liquids for understanding the functionalities or *in operando* performance of an enormous range of materials and systems in the extensive areas of piezoelectric and ferroelectric materials, underwater and related electrical devices, electrochemical systems, and bioelectronics. These theoretical findings and experimental investigations could open up pathways for electrical probing in more complex liquid environments to be extended to more extensive research and to provide insights into the implementation of other advanced techniques in liquid environments.

ACKNOWLEDGMENTS

This work is financially supported by the National Key R&D Program of China (Grants No. 2017YFA0303403 and No. 2018YFB0406500), the National Natural Science Foundation of China (Grants No. 61674057 and No. 91833303), projects of the Science and Technology Commission of Shanghai Municipality (Grants No. 18JC1412400, No. 18YF1407200, and No. 18YF1407000), and the Program for the Professor of Special Appointment (Eastern Scholar) at the Shanghai Institutions of Higher Learning.

Y.Y. and A.Y.C. contributed equally to this work.

APPENDIX A: THEORETICAL ANALYSIS OF ELECTRIC-POTENTIAL DISTRIBUTION IN ELECTROLYTES

More electric-potential behaviors were simulated by the finite element method, in order to clearly demonstrate further the field-screening effect in the tip-surface junction induced by the electric double layer in electrolytes of molarity 10 and 500 m*M* with different valences, as mapped in Fig. 6. The potential is distributed evenly in the 10 m*M* solutions, but shows a tiny drop with increasing valence in Fig. 6(a). In this case, an effective electromechanical interaction between the tip and the sample surface is available during PFM imaging. This allows one to obtain piezoresponse signals in 10 m*M* solutions despite the changing valences. In contrast, as shown in Fig. 6(b), the potential is obviously reduced for higher valences when the molarity of the solutions is 500 m*M*. Additionally, the spatial variations of the electric-potential behavior in the separation between the tip and the surface are given along a vertical distance of 1 nm in Figs. 6(c) and 6(d). Figure 6(c) confirms that the potential is distributed continuously and declines by no more than 5%, contributing to a weak screening effect in the tip-surface junction in 10 m*M* electrolytes, while there is a sharp reduction of the potential of beyond 50% caused by EDLs with increasing valence in 500 m*M* solutions, as plotted in Fig. 6(d). The electromechanical interaction seems to be interrupted in a conductive liquid with high molarity and large valence. Therefore, the field-screening effect resulting from the EDL structure has a great impact on electromechanical imaging by the PFM technique.

We argue that a wider dead layer of several nanometers might exist in the tip-surface system [25]. The potential distribution is also modeled when the thickness of the dead layer is 3 nm in Fig. 7. When the ionic strength increases, the potential decays owing to the field-screening effect, just like the result when the gap is 1 nm. Similarly, the higher valence and concentration create a stronger field-screening

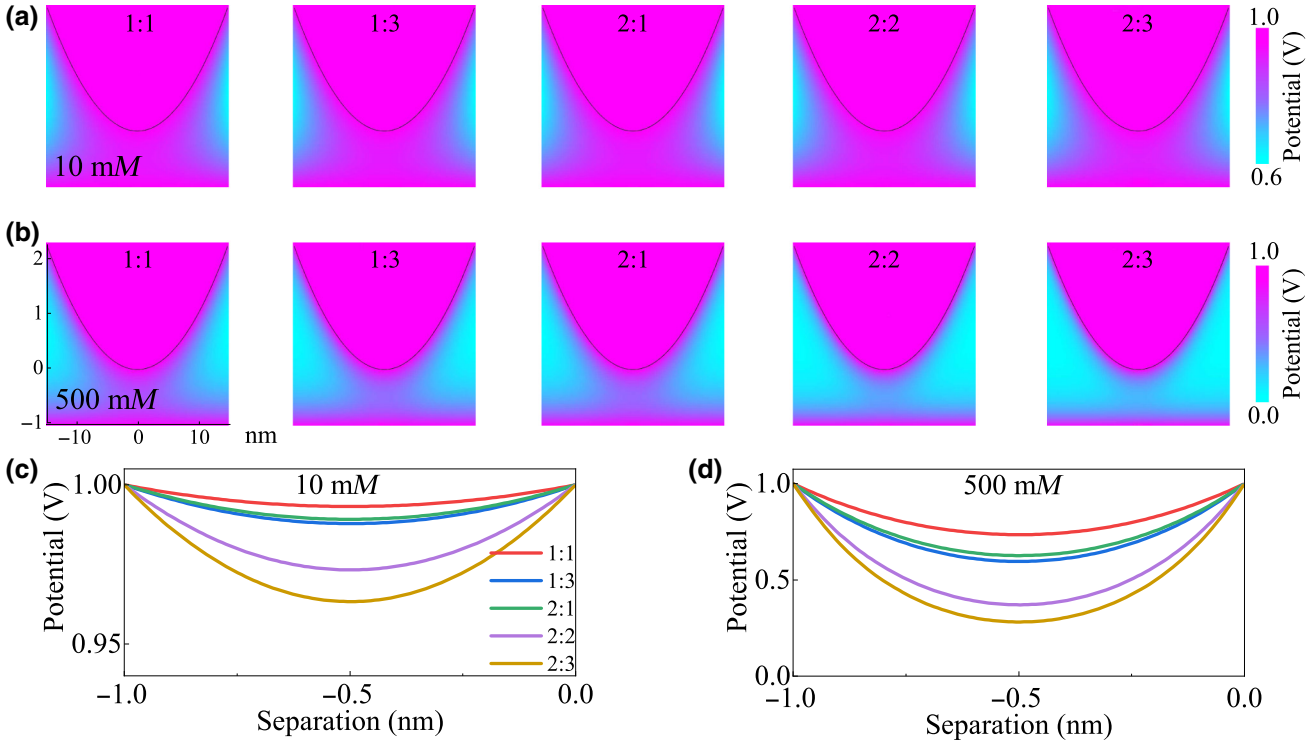

FIG. 6. Electric-potential distributions between tip and sample surface modeled by finite element method in (a) 10 m*M* and (b) 500 m*M* solutions with a variety of valences, when the surface potential is 1 V and the thickness of the dead layer is 1 nm. Lines showing the behavior of the potential distribution along a separation of 1 nm with different types of valence for (c) 10 m*M* solutions and (d) 500 m*M* solutions.

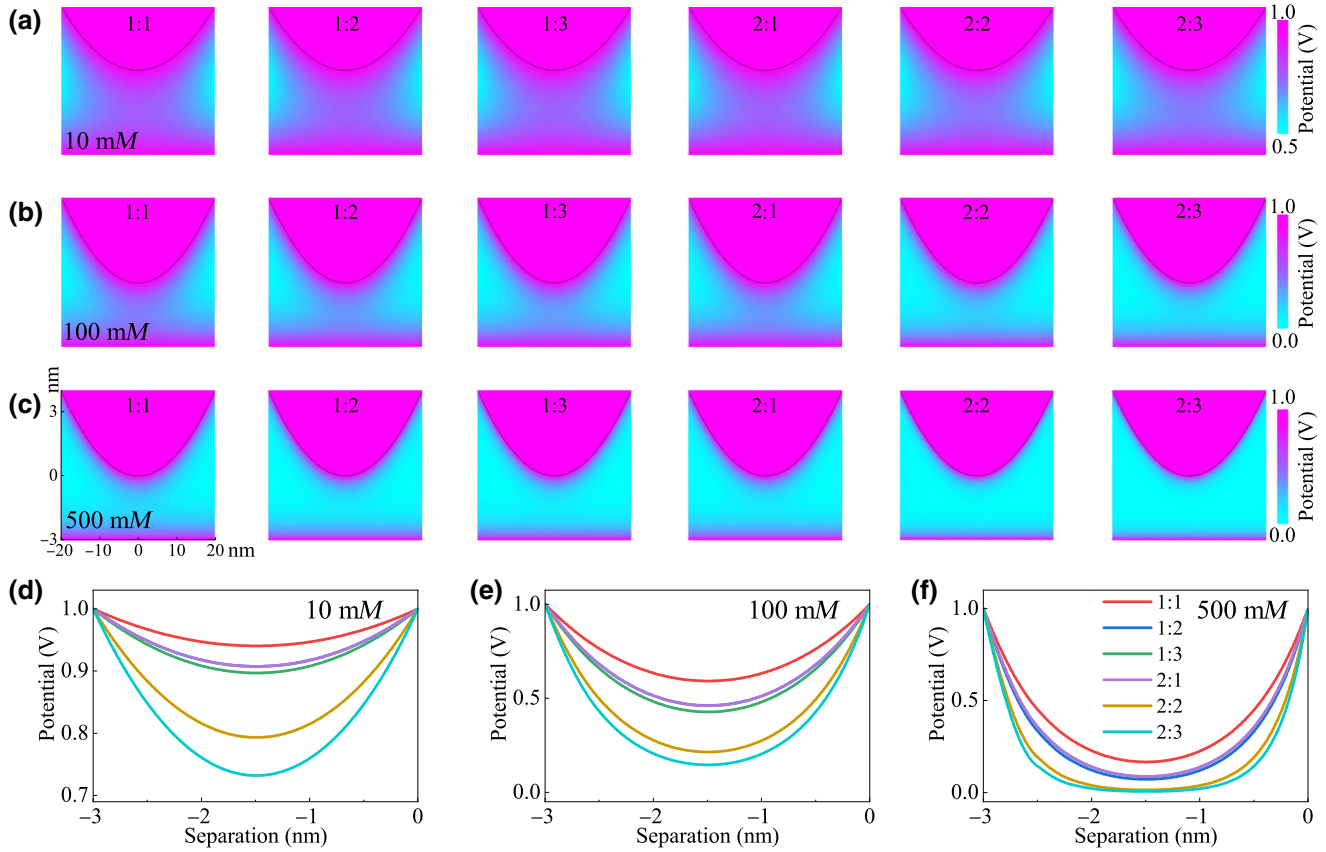

FIG. 7. Electric-potential distributions between tip and sample surface modeled by finite element method in (a) 10 mM, (b) 100 mM, and (b) 500 mM solutions with a variety of valences, when the thickness of the dead layer is 3 nm and the surface potential is 1 V. Lines showing the behavior of the potential distribution along a separation of 3 nm with different types of valence for (d) 10 mM solutions, (e) 100 mM solutions, and (f) 500 mM solutions.

effect, associated with the growing challenge of PFM mapping in highly conductive liquid environments. The spatial variation of the potential along the separation is shown in Figs. 7(d)–7(f). The potential decays by more than 5% in the middle of the dead layer with increasing valence when the molarity of the electrolytes is 10 mM. When the molarity of the electrolytes is raised to 100 mM, the potential declines by over 60%. Furthermore, it can be seen that the potential around $z = 1.5$ nm falls close to 0 V in 500 mM solutions, which means that the delivery of the electric field is almost blocked by the serious field-screening effect. It may be impossible to image electromechanical properties in such electrolytes. The thicker dead layer strengthens the limitation on the concentration of the imaging solutions in PFM measurements.

In addition, simulations are done in which the surface potential of the sample is taken as 0 V while the thickness of the dead layer is 1 nm. The variation of the potential distribution near the tip surface in Figs. 8(a)–8(c) displays a similar screening effect to that in Fig. 2. However, the potential distribution adjacent to the sample surface is around 0 V. Lines showing the behavior of the potential in the tip-sample junction are shown in Figs. 8(d)–8(f). Because the surface potential of the electromechanical sample is considered as 0 V, it requires the spatial distribution of the potential to decrease from 1 V at the tip surface to 0 V. In solutions of molarity 10 mM and low valence, the potential decreases linearly, indicating a robust electric-field distribution. In contrast, a higher conductivity of the electrolyte leads to exponential reduction of the potential in the tip-surface junction. Electromechanical coupling is imaged through amplifying the effective electromechanical interaction between the PFM tip and the surface. However, the theoretical results demonstrate that strong conductivity with high ionic strength may result in an unexpected field-screening effect, blocking the effective piezoresponse signal.

APPENDIX B: LATTICE STRUCTURE ANALYSIS OF PIMNT SINGLE CRYSTAL

A relaxor-based ferroelectric single-crystal 30PIN-35PMN-35PT sample is chosen as the model sample, where the constitution is near the morphotropic phase

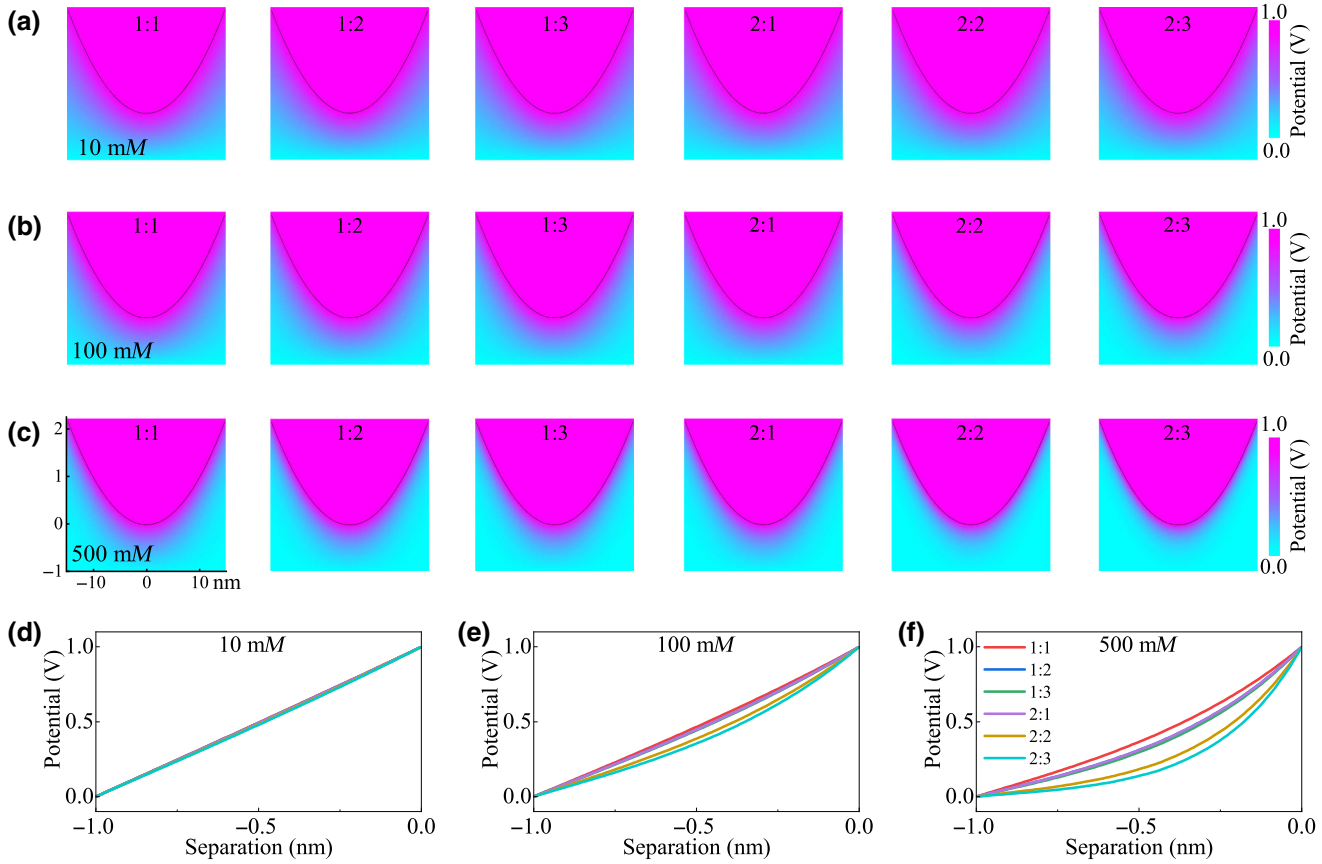

FIG. 8. Electric-potential distributions between tip and sample surface modeled by finite element method in (a) 10 m*M*, (b) 100 m*M*, and (c) 500 m*M* solutions with a variety of valences, when the surface potential is 0 V and the thickness of the dead layer is 1 nm. Lines showing the behavior of the potential distribution between the tip and sample with different types of valence for (d) 10 m*M* solutions, (e) 100 m*M* solutions, and (f) 500 m*M* solutions.

boundary (MPB), as shown in Fig. 9(a). Because of its enhanced dielectric and piezoelectric properties owing to the composition near the MPB and the existence of polar nanoregions [55–57], it is feasible to use it in many applications, such as in (biological) energy-transfer systems and ultrasonic transducers [13,58]. Figure 9(a) represents the phase diagram of PIMNT in a right-handed three-dimensional Cartesian coordinate system, which includes the tetragonal phase of PIMNT. Moreover, the lattice structure of PIMNT in the tetragonal phase (*T*, space group *P*4*mm*) can be evaluated based on x-ray diffraction (XRD) and the Raman spectrum. The Raman spectrum of this

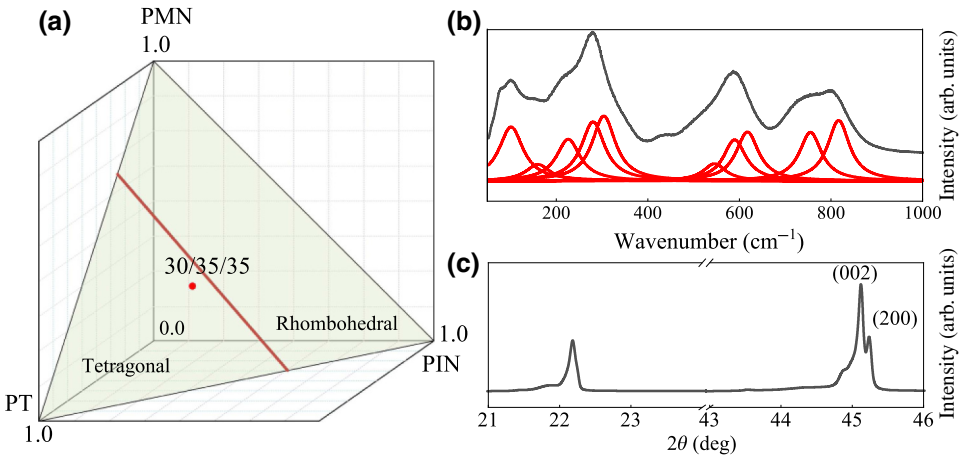

FIG. 9. (a) Phase diagram, (b) Raman spectrum with Lorentzian fitting (red lines) at room temperature from 50 to 1000 cm^{-1}, (c) XRD pattern with a range of 21°–46° of PIMNT (30/35/35) single crystal.

crystal at room temperature is presented with Lorentzian fitting curves in Fig. 9(b). The assignment of phonon modes in the tetragonal phase of PIMNT is plotted [59]. Figure 9(c) shows the (200) diffraction peaks at 2θ from 21° to 46°. At about 45°, it can be observed that two peaks (002)/(200) split from the (200) peak, which means the tetragonal phase is dominant in this crystal [60,61].

APPENDIX C: EXPERIMENTAL METHODS

Experiments on piezoelectric detection in air, deionized water (Milli-Q Advantage, 18.2 MΩ/cm), and K_2SO_4, Na_3PO_4, $CuCl_2$, $MgCl_2$, $MgSO_4$, and glucose solutions with concentrations of 1, 10, 100 m*M* are carried out in a commercial atomic force microscopy system (Dimension Icon, Bruker) equipped with a NanoScope V controller including a functional generator and lock-in amplifier. All experiments are implemented by using an insulated nanoelectrode probe (PFSECM, Bruker) at room temperature. The probe is designed to be fully isolated by dielectric materials except for a Pt-coated tip apex about 43.4 nm in diameter. The spring constant of the cantilever is about 1.5 N/m.

A relaxor-based single crystal of 30PIN-35PMN-35PT is grown by means of a modified vertical Bridgman method [62]. Using PbO, In_2O_3, MgO, Nb_2O_5, and TiO_2 powders (purity higher than 99.99%) as the starting materials, the ingredients are mixed in a certain proportion and presynthesized. After thermal processing in the crucible, the crystal obtained is cut into wafers or bands along the (100) direction [62]. This growth method has been widely used to prepare $PbTiO_3$-based ferroelectric materials of high quality. The lattice structure is analyzed using an x-ray diffractometer (Cu $K\alpha$, D8 Advance, Bruker) with a range of 20°–50°. A micro-Raman spectrometer (Jobin-Yvon LabRAM HR Evolution, Horiba) with a 532 nm excitation laser is used to record the Raman spectrum. The recorded range of wave numbers is from 50 to 1000 cm^{-1}.

[1] J. J. Jiang, Z. Q. Huang, C. X. Xiang, R. Poddar, H. Lewerenz, K. M. Papadantonakis, N. S. Lewis, and B. S. Brunschwig, Nanoelectrical and nanoelectrochemical imaging of Pt/p-Si and Pt/p^+-Si electrodes, ChemSusChem **10**, 4657 (2017).

[2] M. R. Nellist, F. A. L. Laskowski, J. J. Qiu, H. Hajibabaei, K. Sivula, T. W. Hamann, and S. W. Boettcher, Potential-sensing electrochemical atomic force microscopy for in operando analysis of water-splitting catalysts and interfaces, Nat. Energy **3**, 46 (2017).

[3] H. Rokni and W. Lu, Nanoscale probing of interaction in atomically thin layered materials, ACS Cent. Sci. **4**, 288 (2018).

[4] X. Chen, J. Q. Lai, Y. B. Shen, Q. Chen, and L. W. Chen, Functional scanning force microscopy for energy nanodevices, Adv. Mater. **30**, 1802490 (2018).

[5] T. D. Nguyen, N. Deshmukh, J. M. Nagarah, T. Kramer, P. K. Purohit, M. J. Berry, and M. C. McAlpine, Piezoelectric nanoribbons for monitoring cellular deformations, Nat. Nanotech. **7**, 587 (2012).

[6] A. L. Domanski, Kelvin probe force microscopy in nonpolar liquids, Langmuir **28**, 13892 (2012).

[7] M. R. Nellist, F. A. L. Laskowski, J. J. Qiu, H. Hajibabaei, K. Sivula, T. W. Hamann, and S. W. Boettcher, Potential-sensing electrochemical atomic force microscopy for in operando analysis of water-splitting catalysts and interfaces, Nat. Energy **3**, 46 (2018).

[8] E. Soergel, Piezoresponse force microscopy (PFM), J. Phys. D: Appl. Phys. **44**, 464003 (2011).

[9] A. Y. Cui, K. Jiang, P. Zhang, L. P. Xu, G. S. Xu, X. M. Chen, Z. G. Hu, and J. H. Chu, In situ exploration of thermal-induced domain evolution with phase transition in $LiNbO_3$-Modified $K_{0.5}Na_{0.5}NbO_3$ single crystal, J. Phys. Chem. C **121**, 14322 (2017).

[10] D. Rossi, A. Pecchia, M. A. der Maur, T. Leonhard, H. Röhm, M. J. Hoffmann, A. Colsmann, and A. D. Carlo, On the importance of ferroelectric domains for the performance of perovskite solar cells, Nano Energy **48**, 20 (2018).

[11] S. W. Wang, Q. Liu, C. L. Zhao, F. Z. Lv, X. Y. Qin, H. D. Du, F. Y. Kang, and B. H. Li, Advances in understanding materials for rechargeable lithium batteries by atomic force microscopy, Energy Environ. Mater. **1**, 28 (2018).

[12] H. Bülter, F. Peters, J. Schwenzel, and G. Wittstock, Spatiotemporal changes of the solid electrolyte interphase in lithium-ion batteries detected by scanning electrochemical microscopy, Angew. Chem. Int. Ed. **53**, 10531 (2014).

[13] G.-T. Hwang, Y. Kim, J.-H. Lee, S. Oh, C. K. Jeong, D. Y. Park, J. Ryu, H. Kwon, S.-G. Lee, B. Joung, D. Kim, and K. J. Lee, Self-powered deep brain stimulation via a flexible PIMNT energy harvester, Energy Environ. Sci. **8**, 2677 (2015).

[14] G.-T. Hwang, H. Park, J.-H. Lee, S. Oh, K. Park, M. Byun, H. Park, G. Ahn, C. K. Jeong, K. No, H. Kwon, S.-G. Lee, B. Joung, and K. J. Lee, Self-powered cardiac pacemaker enabled by flexible single crystalline PMN-PT piezoelectric energy harvester, Adv. Mater. **26**, 4880 (2017).

[15] F. Rubio-Marcos, A. D. Campo, R. López-Juárez, J. J. Romero, and J. F. Fernández, High spatial resolution structure of $(K, Na)NbO_3$ lead-free ferroelectric domains, J. Mater. Chem. **22**, 9714 (2012).

[16] Y. Zhang, Y. Zhang, Q. Guo, X. L. Zhong, Y. H. Chu, H. D. Lu, G. K. Zhong, J. Jiang, C. B. Tan, M. Liao, Z. H. Lu, D. W. Zhang, J. B. Wang, J. M. Yuan, and Y. C. Zhou, Characterization of domain distributions by second harmonic generation in ferroelectrics, npj Comput. Mater. **4**, 39 (2018).

[17] J. Kim, J. Hong, M. Park, W. Zhe, D. Kim, Y. J. Jang, D. H. Kim, and K. No, Facile preparation of $PbTiO_3$ nanodot arrays: Combining nanohybridization with vapor phase reaction sputtering, Adv. Funct. Mater. **21**, 4277 (2011).

[18] S. M. Griffin, M. Lilienblum, K. T. Delaney, Y. Kumagai, M. Fiebig, and N. A. Spaldin, Scaling Behavior and Beyond Equilibrium in the Hexagonal Manganites, Phys. Rev. X **2**, 041022 (2012).

[19] P. Jiang, F. Yan, E. N. Esfahani, S. H. Xie, D. F. Zou, X. Y. Liu, H. R. Zheng, and J. Y. Li, Electromechanical

coupling of murine lung tissues probed by piezoresponse force microscopy, ACS Biomater. Sci. Eng. **3**, 1827 (2017).

[20] Y. M. Liu, Y. H. Zhang, M. Chow, Q. N. Chen, and J. Y. Li, Biological Ferroelectricity Uncovered in Aortic Walls by Piezoresponse Force Mcroscopy, Phys. Rev. Lett. **108**, 078103 (2012).

[21] Y. M. Liu, H.-L. Cai, M. Zelisko, Y. J. Wang, J. L. Sun, F. Yan, F. Y. Ma, P. Q. Wang, Q. N. Chen, H. R. Zheng, X. J. Meng, P. Sharma, Y. H. Zhang, and J. Y. Li, Ferroelectric switching of elastin, PNAS **111**, E2780 (2014).

[22] A. Y. Cui, P. De Wolf, Y. Ye, Z. G. Hu, A. Dujardin, Z. Q. Huang, K. Jiang, L. Y. Shang, M. Ye, H. Sun, and J. H. Chu, Probing electromechanical behaviors by datacube piezoresponse force microscopy in ambient and aqueous environments, Nanotechnology **30**, 235701 (2019).

[23] B. J. Rodriguez, S. Jesse, A. P. Baddorf, and S. V. Kalinin, High Resolution Electromechanical Imaging of Ferroelectric Materials in a Liquid Environment by Piezoresponse Force Microscopy, Phys. Rev. Lett. **96**, 237602 (2006).

[24] B. J. Rodriguez, S. Jesse, A. P. Baddorf, S. Kim, and S. V. Kalinin, Controlling Polarization Dynamics in a Liquid Environment: From Localized to Macroscopic Switching in Ferroelectrics, Phys. Rev. Lett. **98**, 247603 (2007).

[25] N. Balke, A. Tselev, T. M. Arruda, S. Jesse, Y. Chu, and S. V. Kalinin, Probing local electromechanical effects in highly conductive electrolytes, ACS Nano **6**, 10139 (2012).

[26] N. Balke, S. Jesse, Y.-H. Chu, and S. V. Kalinin, High-frequency electromechanical imaging of ferroelectrics in a liquid environment, ACS Nano **6**, 5559 (2012).

[27] M. P. N. Ikiforov, G. L. Thompson, V. V. Reukov, S. Jesse, S. Guo, B. J. Rodriguez, K. Seal, A. A. Vertegel, and S. V. Kalinin, Double-layer mediated electromechanical response of amyloid fibrils in liquid environment, ACS Nano **4**, 689 (2010).

[28] G. L. Thompson, V. V. Reukov, M. P. Nikiforov, S. Jesse, S. V. Kalinin, and A. A. Vertegel, Electromechanical and elastic probing of bacteria in a cell culture medium, Nanotechnology **23**, 245705 (2012).

[29] S. V. Kalinin, B. J. Rodriguez, S. Jesse, K. Seal, R. Proksch, S. Hohlbauch, I. Revenko, G. L. Thompson, and A. A. Vertegel, Towards local electromechanical probing of cellular and biomolecular systems in a liquid environment, Nanotechnology **18**, 424020 (2007).

[30] L. Collins, J. I. Kilpatrick, S. V. Kalinin, and B. J. Rodriguez, Towards nanoscale electrical measurements in liquid by advanced KPFM techniques: A review, Rep. Prog. Phys. **81**, 086101 (2018).

[31] K. Umeda, K. Kobayashi, N. Oyabu, Y. Hirata, K. Matsushige, and H. Yamada, Practical aspects of Kelvin-probe force microscopy at solid/liquid interfaces in various liquid media, J. Appl. Phys. **116**, 134307 (2014).

[32] A. Y. Cui, L. Q. Zhu, K. Jiang, L. P. Xu, Z. G. Hu, G. S. Xu, H. Sun, Z. Q. Huang, R. Poddar, and J. H. Chu, Probing Nanoscale Electromechanical Behaviors of Relaxor Ferroelectrics in Highly Conductive Liquid Environments, Phys. Rev. Appl. **11**, 054037 (2019).

[33] A. Gruverman, M. Alexe, and D. Meier, Piezoresponse force microscopy and nanoferroic phenomena, Nat. Commun. **10**, 1661 (2019).

[34] R. K. Vasudevan, N. Balke, P. Maksymovych, S. Jesse, and S. V. Kalinin, Ferroelectric or non-ferroelectric: Why so many materials exhibit "ferroelectricity" on the nanoscale, Appl. Phys. Rev. **4**, 021302 (2017).

[35] Q. Li, Y. Liu, D. Y. Wang, R. L. Withers, Z. R. Li, H. S. Luo, and Z. Xu, Switching spectroscopic measurement of surface potentials on ferroelectric surfaces via an open-loop Kelvin probe force microscopy method, Appl. Phys. Lett. **101**, 242906 (2012).

[36] J. N. Israelachvili, *Intermolecular and Surface Forces* (Elsevier Pte Ltd., Singapore, 2011). Chap. *14*.

[37] A. J. Bard and L. R. Faulkner, *Electrochemical Methods: Fundamentals and Applications* (John Wiley & Sons, Inc., New York, 2000). Chaps. *1 & 13*.

[38] J. H. Masliyah and S. Bhattacharjee, *Electrokinetic and Colloid Transport Phenomena* (John Wiley & Sons, Inc., New York, 2006). Chap. *5*.

[39] R. J. Ferris, S. H. Lin, M. Therezien, B. B. Yellen, and S. Zauscher, Electric double layer formed by polarized ferroelectric thin films, ACS Appl. Mater. Interfaces **5**, 2610 (2013).

[40] J. Sotres, A. Lostaob, C. Gómez-Morenoc, and A. M. Baró, Jumping mode AFM imaging of biomolecules in the repulsive electrical double layer, Ultramicroscopy **107**, 1207 (2007).

[41] J. Sotres and A. M. Baró, AFM imaging and analysis of electrostatic double layer forces on single DNA molecules, Biophys. J. **98**, 1995 (2010).

[42] K. Umeda, K. Kobayashi, N. Oyabu, K. Matsushige, and H. Yamada, Molecular-scale quantitative charge density measurement of biological molecule by frequency modulation atomic force microscopy in aqueous solutions, Nanotechnology **26**, 285103 (2015).

[43] M. Liu, Y. J. Pang, B. Zhang, P. De Luna, O. Voznyy, J. X. Xu, X. L. Zheng, C. T. Dinh, F. J. Fan, C. H. Cao, F. Pelayo, G. de Arquer, T. S. Safaei, A. Mepham, A. Klinkova, E. Kumacheva, T. Filleter, D. Sinton, S. O. Kelley, and E. H. Sargent, Enhanced electrocatalytic CO_2 reduction via field-induced reagent concentration, Nature **537**, 382 (2016).

[44] L. Collins, S. Jesse, J. I. Kilpatrick, A. Tselev, O. Varenyk, M. B. Okatan, S. A. L. Weber, A. Kumar, N. Balke, S. V. Kalinin, and B. J. Rodriguez, Probing charge screening dynamics and electrochemical processes at the solid-liquid interface with electrochemical force microscopy, Nat. Commun. **5**, 3871 (2014).

[45] J. H. Noh, M. Nikiforov, S. V. Kalinin, A. A. Vertegel, and P. D. Rack, Nanofabrication of insulated scanning probes for electromechanical imaging in liquid solutions, Nanotechnology **21**, 365302 (2010).

[46] Z. Q. Huang, P. De Wolf, R. Poddar, C. Z. Li, A. Mark, M. R. Nellist, Y. K. Chen, J. J. Jiang, G. Papastavrou, S. W. Boettcher, C. X. Xiang, and B. S. Brunschwig, PeakForce scanning electrochemical microscopy with nanoelectrode probes, Micros. Today **24**, 18 (2016).

[47] M. R. Nellist, Y. K. Chen, A. Mark, S. Gödrich, C. Stelling, J. J. Jiang, R. Poddar, C. Z. Li, R. Kumar, G. Papastavrou, M. Retsch, B. S. Brunschwig, Z. Q. Huang, C. X. Xiang, and S. W. Boettcher, Atomic force microscopy with nanoelectrode tips for high resolution electrochemical, nanoadhesion and nanoelectrical imaging, Nanotechnology **28**, 095711 (2017).

[48] M. Abplanalp, D. Barošová, P. Bridenbaugh, J. Erhart, J. Fousek, P. Günter, J. Nosek, and M. Šulc, Scanning force

microscopy of domain structures in $Pb(Zn_{1/3}Nb_{2/3})O_3 - 8\%PbTiO_3$ and $Pb(Mg_{1/3}Nb_{2/3})O_3 - 29\%PbTiO_3$, J. Appl. Phys. **91**, 3797 (2002).

[49] M. C. Shin, S. J. Chung, S. Lee, and R. S. Feigelson, Growth and observation of domain structure of lead magnesium niobate-lead titanate single crystals, J. Cryst. Growth **263**, 412 (2004).

[50] F. Bai, J. Li, and D. Viehland, Domain engineered states over various length scales in (001)-Oriented $Pb(Mg_{1/3}Nb_{2/3})O_{3-x}\%PbTiO_3$ crystals: Electrical history dependence of hierarchal domains, J. Appl. Phys. **97**, 054103 (2005).

[51] A. Hubert and R. Schäfer, *Magnetic Domains* (Springer, Berlin, 1998).

[52] M. Bode, Spin-polarized scanning tunnelling microscopy, Rep. Prog. Phys. **66**, 523 (2003).

[53] A. Gruverman, O. Auciello, and H. Tokumoto, Imaging and control of domain structures in ferroelectric thin films via scanning force microscopy, Annu. Rev. Mater. Sci. **28**, 101 (1998).

[54] D. J. Müller, F. A. Schabert, G. Büldt, and A. Engel, Imaging purple membranes in aqueous solutions at sub-nanometer resolution by atomic force microscopy, Biophys. J. **68**, 1681 (1995).

[55] F. Li, S. J. Zhang, T. N. Yang, Z. Xu, N. Zhang, G. Liu, J. J. Wang, J. L. Wang, Z. X. Cheng, Z.-G. Ye, J. Luo, T. R. Shrout, and L.-Q. Chen, The origin of ultrahigh piezoelectricity in relaxor-ferroelectric solid solution crystals, Nat. Commun. **7**, 13807 (2016).

[56] G. Y. Xu, J. S. Wen, C. Stock, and P. M. Gehring, Phase instability induced by polar nanoregions in a relaxor ferroelectric system, Nat. Mater. **7**, 562 (2008).

[57] M. E. Manley, D. L. Abernathy, R. Sahul, D. E. Parshall, J. W. Lynn, A. D. Christianson, P. J. Stonaha, E. D. Specht, and J. D. Budai, Giant electromechanical coupling of relaxor ferroelectrics controlled by polar nanoregion vibrations, Sci. Adv. **2**, e1501814 (2016).

[58] S. Zhang and F. Li, High performance ferroelectric relaxor-$PbTiO_3$ single crystals: Status and perspective, J. Appl. Phys. **111**, 031301 (2012).

[59] J. J. Zhu, K. Jiang, G. S. Xu, Z. G. Hu, Y. W. Li, Z. Q. Zhu, and J. H. Chu, Temperature-dependent Raman scattering and multiple phase coexistence in relaxor ferroelectric $Pb(In_{1/2}Nb_{1/2})O_3 - Pb(Mg_{1/3}Nb_{2/3})O_3 - PbTiO_3$ single crystals, J. Appl. Phys. **114**, 153508 (2013).

[60] D. Wang, M. Cao, and S. Zhang, Phase diagram and properties of $Pb(In_{1/2}Nb_{1/2})O_3 - Pb(Mg_{1/3}Nb_{2/3})O_3 - PbTiO_3$ polycrystalline ceramics, J. Eur. Ceram. Soc. **32**, 433 (2012).

[61] N. Luo, Q. Li, Z. Xia, and X. Chu, Phase diagram, temperature stability, and electrical properties of $(0.85 - x)Pb(Mg_{1/3}Nb_{2/3})O_3 - 0.10Pb(Fe_{1/2}Nb_{1/2})O_3 - 0.05PbZrO_3 - xPbTiO_3$ system, J. Am. Ceram. Soc. **95**, 3246 (2012).

[62] G. S. Xu, K. Chen, D. F. Yang, and J. B. Li, Growth and electrical properties of large size $Pb(In_{1/2}Nb_{1/2})O_3 - Pb(Mg_{1/3}Nb_{2/3})O_3 - PbTiO_3$ crystals prepared by the vertical Bridgman technique, Appl. Phys. Lett. **90**, 032901 (2007).